

# Synthesis, spectroscopic (FT–IR and UV–Vis), crystallographic and theoretical studies, and a molecular docking simulation of an imatinib-like template

Rodolfo Moreno-Fuquen,<sup>a\*</sup> Kevin Arango-Daraviña,<sup>a</sup> Esteban Garcia,<sup>a</sup> Juan-C. Tenorio<sup>b</sup> and Javier Ellena<sup>b</sup>

Received 1 September 2019

Accepted 17 November 2019

Edited by A. R. Kennedy, University of Strathclyde, Scotland

**Keywords:** imatinib-like; crystal structure; molecular docking simulation; computational chemistry; pyrimidinamine.

**CCDC reference:** 1966319

**Supporting information:** this article has supporting information at journals.iucr.org/c

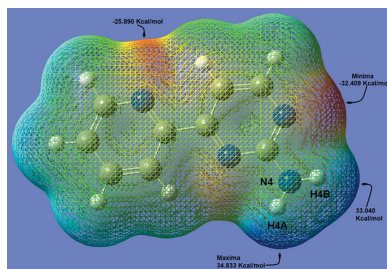
<sup>a</sup>Grupo de Cristalografía, Departamento de Química, Universidad del Valle, AA 25360, Santiago de Cali, Colombia, and <sup>b</sup>Instituto de Física de São Carlos, IFSC, Universidade de São Paulo, USP, São Carlos, SP, Brazil. \*Correspondence e-mail: rodolfo.moreno@correounivalle.edu.co

The aim of the present study was to report the crystal structure and spectroscopic, electronic, supramolecular and electrostatic properties of a new polymorph of 4-(pyridin-2-yl)pyrimidin-2-amine ( $C_9H_8N_4$ ). The compound was synthesized under microwave irradiation. The single-crystal X-ray structure analysis revealed an angle of  $13.36(8)^\circ$  between the planes of the rings, as well as molecules linked by  $Nsp^2-H \cdots N$  hydrogen bonds forming dimers along the crystal. The material was analyzed by FT–IR vibrational spectroscopy, while a computational approach was used to elucidate the vibrational frequency couplings. The existence of  $Nsp^2-H \cdots N$  hydrogen bonds in the crystal was confirmed spectroscopically by the IR peaks from the N–H stretching vibration shifting to lower wavenumbers in the solid state relative to those in the gas phase. The supramolecular studies confirmed the formation of centrosymmetric  $R_2^2(8)$  rings, which correspond to the formation of dimers that stack parallel to the *b* direction. Other weak  $C-H \cdots \pi$  interactions, essential for crystal growth, were found. The UV–Vis spectroscopic analysis showed a donor–acceptor process, where the amino group acts as a donor and the pyridine and pyrimidine rings act as acceptors. The reactive sites of the molecule were identified and their quantitative values were defined using the electrostatic potential model proposed in the multifunctional wave function analyzer *multiwfn*. The calculated interaction energies between pairs of molecules were used to visualize the electrostatic terms as the leading factors against the dispersion factors in the crystal-growth process. The docking results showed that the amino group of the pyrimidine moiety was simultaneously anchored by hydrogen-bonding interactions with the Asp427 and His407 protein residues. This compound could be key for the realization of a series of syntheses of molecules that could be used as possible inhibitors of chronic myelogenous leukemia.

## 1. Introduction

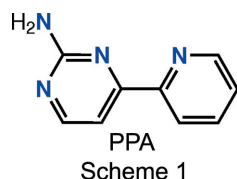
The pyrimidine system is a six-membered organic heterocycle with N atoms at positions 1 and 3 of the ring (Brown, 2009; Padwa *et al.*, 1984). Pyrazine and pyridazine, other diazines, have N atoms at different positions in the ring. Of the nucleic acids, three nucleobases are pyrimidine derivatives, namely pyrimidine-2,4(1*H*,3*H*)-dione (Zajac *et al.*, 2003), 5-methylpyrimidine-2,4(1*H*,3*H*)-dione (Joule & Mills, 2010) and 4-aminopyrimidin-2(1*H*)-one (Chahwan *et al.*, 2010).

The presence of a pyrimidine skeleton in thymine, cytosine and uracil, which are essential building blocks of DNA and RNA nucleic acids, may be one of the reasons why pyrimidine products are so widely used in therapeutic applications. This work seeks to study a system that can include the character-



© 2019 International Union of Crystallography

istics of pyrimidine and pyridine as a whole, *i.e.* 4-(pyridin-2-yl)pyrimidin-2-amine (hereafter **PPA**). The presence of the pyrimidine ring covalently bound to pyridine makes it a very attractive scaffold for the synthesis of diverse products that can exhibit very interesting biological and chemical properties. The importance of the pyrimidine nucleus can be appreciated since it is related to many vital molecules, such as thiamine (Bettendorff *et al.*, 1996, 2007), riboflavin (Zempleni *et al.*, 1996) and folic acid (Bailey & Ayling, 2009). In addition, the pyrimidine skeleton is present in many synthetic compounds, such as barbituric acid, and in compounds such as veranal, which is used in hypnosis (Porter, 1979). Many pyrimidine derivatives have antibacterial (Sharma *et al.*, 2004), antifungal (Agarwal *et al.*, 2000), analgesic (Sondhi *et al.*, 2008), anti-inflammatory (Amir *et al.*, 2007), antihypertensive (Rana *et al.*, 2004) or anticancer activities (Xie *et al.*, 2009). In this work, the structure of **PPA** (Scheme 1) was investigated using both theoretical studies and X-ray crystallography.



## 2. Experimental

### 2.1. Structure and spectra

The reactions were monitored by thin-layer chromatography (TLC). The melting points were determined on a Büchi melting point B-450 apparatus. The IR spectra were recorded on a Shimadzu IR Affinity-1 FT-IR coupled with a Pike Miracle ATR. The NMR spectra were recorded on a Bruker Avance 400 spectrometer operating at 400.13 MHz for  $^1\text{H}$  and 100.61 MHz for  $^{13}\text{C}$ , using chloroform-*d* as the solvent and tetramethylsilane (TMS) as the internal standard. Chemical shifts ( $\delta$ ) are reported in ppm, coupling constants (*J*) in Hertz (Hz) and classical abbreviations are used to describe the signal multiplicities. The UV-Vis absorption spectrum of **PPA** was obtained in acetonitrile solution at room temperature in the range 200–600 nm using a UV-Vis Shimadzu 1700 spectrophotometer. Chemicals and solvents were purchased from Sigma-Aldrich and were used without further purification.

### 2.2. Synthesis and crystallization

A mixture of enaminone **1** (1 equiv.), guanidine **2** (1.05 equiv.), sodium hydroxide (1.17 equiv.) and propanol was subjected to microwave radiation at 150 W for 10 min at 95 °C. The crude product obtained was extracted with ethyl acetate (3 × 50 ml). TLC monitoring ( $\text{Cl}_2\text{CH}_2/\text{MeOH}$ , 40:1 *v/v*) revealed the presence of a unique product. Compound **3** (grey colour) was finally obtained in a yield of 80.72% (m.p. 140 °C) (see Scheme 2).

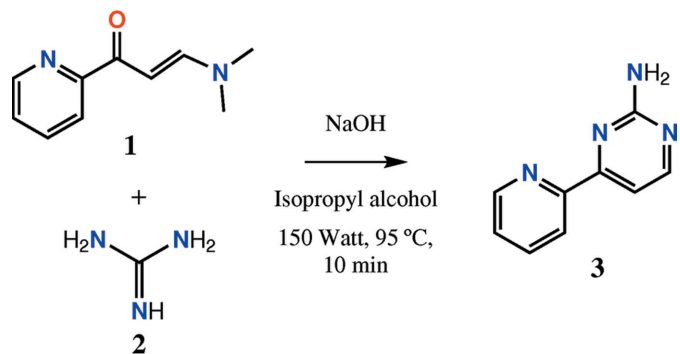
$^1\text{H}$  NMR (400 MHz, chloroform-*d*):  $\delta$  8.69 (*dd*, *J* = 4.7, 1.7 Hz, 1H), 8.43 (*d*, *J* = 5.2 Hz, 1H), 8.31 (*d*, *J* = 7.9 Hz, 1H),

**Table 1**  
Experimental details.

Crystal data	
Chemical formula	$\text{C}_9\text{H}_8\text{N}_4$
$M_r$	172.19
Crystal system, space group	Monoclinic, <i>I2/a</i>
Temperature (K)	293
<i>a</i> , <i>b</i> , <i>c</i> (Å)	11.4608 (15), 5.3791 (9), 26.740 (4)
$\beta$ (°)	91.457 (12)
<i>V</i> (Å <sup>3</sup> )	1647.9 (4)
<i>Z</i>	8
Radiation type	Mo $K\alpha$
$\mu$ (mm <sup>-1</sup> )	0.09
Crystal size (mm)	0.40 × 0.23 × 0.20
Data collection	
Diffractometer	Bruker Enraf-Nonius KappaCCD
Absorption correction	Gaussian ( <i>SADABS</i> ; Bruker, 2012)
$T_{\min}$ , $T_{\max}$	0.624, 0.995
No. of measured, independent and observed [ <i>I</i> > 2σ( <i>I</i> )] reflections	4441, 2379, 1688
$R_{\text{int}}$	0.020
(sin $\theta/\lambda$ ) <sub>max</sub> (Å <sup>-1</sup> )	0.703
Refinement	
$R[F^2 > 2\sigma(F^2)]$ , $wR(F^2)$ , <i>S</i>	0.046, 0.134, 1.03
No. of reflections	2379
No. of parameters	126
H-atom treatment	H atoms treated by a mixture of independent and constrained refinement
$\Delta\rho_{\text{max}}$ , $\Delta\rho_{\text{min}}$ (e Å <sup>-3</sup> )	0.22, -0.22

Computer programs: *DATCOL* (Bruker, 2006), *EVALCCD* (Duisenberg *et al.*, 2003), *SHELXT* (Sheldrick, 2015a), *SHELXL2014* (Sheldrick, 2015b), *ORTEP-3* (Farrugia, 2012), *Mercury* (Macrae *et al.*, 2008) and *CrystalExplorer* (McKinnon *et al.*, 2004).

7.81 (*td*, *J* = 7.8, 1.8 Hz, 1H), 7.62 (*d*, *J* = 5.1 Hz, 1H), 7.36 (*dd*, *J* = 7.5, 4.8 Hz, 1H), 5.33 (*s*, 2H,  $\text{NH}_2$ ).  $^{13}\text{C}$  NMR (100 MHz, chloroform-*d*):  $\delta$  164.23, 163.29, 159.49, 154.48, 149.57, 137.07, 125.19, 121.61, 108.18. IR (FT-IR): 3469.94, 3296.35, 3136.61, 1651.07, 1614.42, 1566.20, 1544.98, 1463.97, 1431.18, 1342.46, 1301.95, 1242.16, 1211.30, 1103.28, 1093.64, 846.75, 804.32, 783.10, 742.59, 650.01.



### 2.3. Refinement

The collected crystal data and structure refinement details of **PPA** are summarized in Table 1. H atoms on C atoms were placed in calculated positions (C–H = 0.93 Å) and were refined using a riding-model approximation, with  $U_{\text{iso}}(\text{H}) = 1.2U_{\text{eq}}(\text{parent})$ . The H atoms of the amine group were refined isotropically.

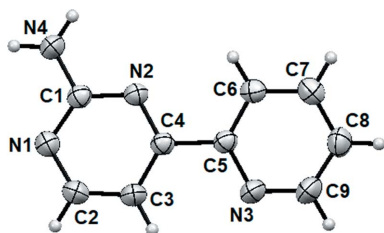


Figure 1

The molecular structure of **PPA**, with displacement ellipsoids drawn at the 50% probability level. H atoms are shown as spheres of arbitrary radii.

## 2.4. Computational study

All theoretical calculations were performed on the system in the gas phase using Becke's three-parameter hybrid functional (B3) (Becke, 1993) with the LYP correlation functional (B3LYP) (Lee *et al.*, 1988) and the 6-311G++(d,p) basis set. The geometry optimization of the molecule was followed by frequency calculations to prove that the energy minimum had been found. The vibrational wavenumber assignments were performed using the *VEDA4* program (Jamróz, 2013) and the vibrations were visualized with the aid of *GaussView* (Version 5.0.8; Nielsen & Holder, 2009).

## 3. Results and discussion

### 3.1. Single-crystal X-ray analysis

The amino group is *anti* with respect to the pyridine N3 atom. The N2—C4—C5—N3 torsion angle is  $-167.20(12)^\circ$ . The planes of the rings of the **PPA** molecule form a dihedral angle of  $13.36(8)^\circ$ . All bond lengths, bond angles and intermolecular distances were found to be normal. The X-ray diffraction analysis confirmed the proposed structure and is depicted in Fig. 1.

### 3.2. Supramolecular features

The projection of the molecular structure, which is generally related to atoms and covalent bonds, towards a level dominated by noncovalent interactions should lead to the use of new rules governing these supramolecular structures and their

Table 2

Hydrogen-bond geometry ( $\text{\AA}$ ,  $^\circ$ ).

$D-H\cdots A$	$D-H$	$H\cdots A$	$D\cdots A$	$D-H\cdots A$
$N4-H4B\cdots N1^i$	0.91 (2)	2.10 (2)	3.0154 (19)	175.8 (16)

Symmetry code: (i)  $-x + 1, -y + 2, -z + 1$ .

dynamics, transformations and molecular assembly properties. It is therefore interesting to undertake a supramolecular study of **PPA** to find the noncovalent relationships governing its supramolecular structure (Turro, 2005). The noncovalent bonds most frequently discussed in biological systems are hydrogen bonds. Several properties observed in these systems depend on interactions with neighbouring molecules. The formation of dimers, rings or infinite chains of molecules, generated by hydrogen bonds, affects the properties of these biological systems. In this particular system, the formed N—H $\cdots$ N interactions are evocative of the interactions between complementary DNA base pairs. Other weaker interactions, such as  $N4-H4A\cdots C3$ , that complement crystalline formation, are also observed. The  $N4-H4B$  group acts as a hydrogen-bond donor for atom  $N1^i$  (Table 2), forming hydrogen-bonding dimers with  $R_2^2(8)$  graph-set motifs. These rings afford dimers at the supramolecular level and each dimer forms an approximate right angle with the next dimer as they run along the [001] direction (Fig. 2). The formation of this kind of dimer is characteristic of the crystal growth of pyrimidine compounds. The crystal packing also features weak C—H $\cdots\pi$  interactions. This weak attractive force may play an important role in various fields of biology or chemistry (Nakamura *et al.*, 1982; Sakaki *et al.*, 1993). The C8—H8 group shows an interaction with the centroid of the pyridine ring in the molecule with the symmetry code  $(-x + 1, y - \frac{1}{2}, -z + \frac{3}{2})$ , with a distance from the H8 atom to the ring centroid of 2.95  $\text{\AA}$ .

### 3.3. Hirshfeld surfaces

Hydrogen-bond interactions enhance the stability of the supramolecular structure and this behaviour can be explored through Hirshfeld surface analysis using the *CrystalExplorer* program (Spackman & Jayatilaka, 2009), which allows the

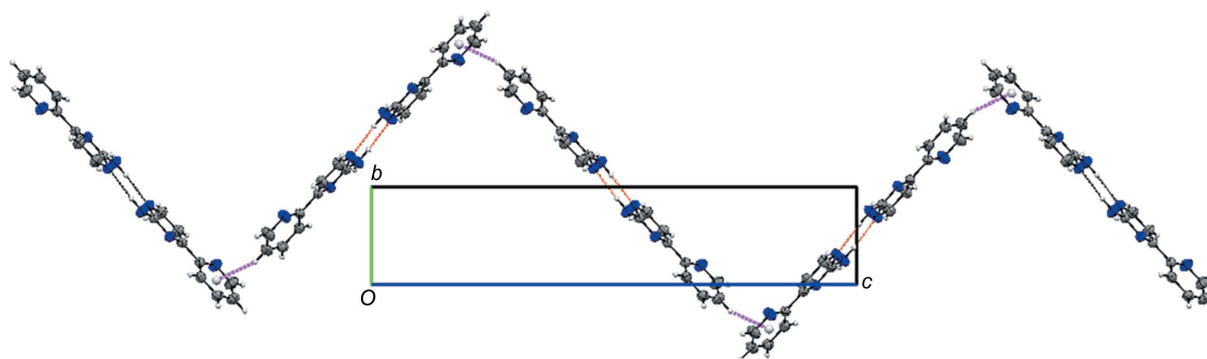


Figure 2

Partial crystal structure of **PPA**, showing the formation of dimers linked by N—H $\cdots$ N hydrogen bonds, as well as chains of dimers linked by C—H $\cdots$ Cg interactions (Cg is the centroid of the pyridine ring), running along [001]. [Symmetry codes: (i)  $-x + 1, -y + 2, -z + 1$ ; (ii)  $-x + 1, y - \frac{1}{2}, -z + \frac{3}{2}$ ]

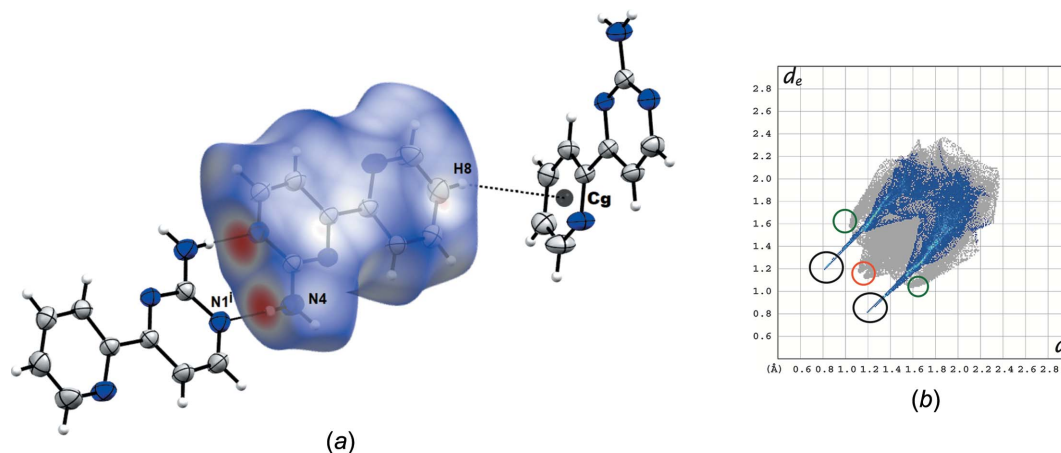


Figure 3

(a)  $d_{\text{norm}}$  surfaces displaying the pairwise N...H interactions and the C—H...Cg interactions (Cg is the centroid of the pyridine ring). (b) Fingerprint plot with the characteristic interactions circled, showing N...H in black, C...H in green and H...H in red.

visualization of the different types of interactions within the crystal structure, including N...H and C...H interactions. Assigning  $d_e$  and  $d_i$  as the external and internal distances of an atom to the Hirshfeld surface and normalizing these pairs of values with respect to the van der Waals (vdW) radii of the corresponding atoms results in the so-called  $d_{\text{norm}}$  surface. Contacts smaller than the sum of the vdW radii of the two atoms result in a negative value, and negative values are highlighted on the surface in red. Contacts close to the limit of the vdW radii are shown in white, and those contacts greater than the sum of the vdW radii are highlighted on the surface in blue (see Fig. 3a).

The Hirshfeld surface  $d_{\text{norm}}$  (in red) indicates the locations of the strongest intermolecular contacts, e.g. the H4B and H7 atoms, which form the most important interactions in the molecule (Fig. 3a). When mapping  $d_e$  and  $d_i$  on this surface, these two values are associated, resulting in relations that are combined in intervals of 0.01 Å, providing the so-called fingerprint. The Hirshfeld surface analysis for **PPA** shows that the N...H and H...N interactions, which appeared as spikes and are indicated by black circles (Fig. 3b), together comprise

24.2% of the total surface. The C...H and H...C interactions combined, which appear as spikes and are indicated by green circles, comprise 8.4% of the surface, and H...H interactions, indicated by red circles, comprise 45.3% of the Hirshfeld surface. The results of the  $d_{\text{norm}}$  surface coincide with the results of the fingerprint plot.

### 3.4. Molecular electrostatic potential (MEP)

The MEP is the potential that a positive charge unit would experience at any point surrounding the molecule due to the electron-density distribution in the molecule. The MEP was used to clarify the interactions among **PPA** molecules, as well as the most important reactive sites on the molecule that could be used in later syntheses. Regions with high negative potentials have a high probability of performing nucleophilic attacks or undergoing protonation reactions, and such sites were identified around the N1 and N3 atoms, which showed MEPs equal to  $-32.409$  and  $-25.890$  kcal mol $^{-1}$ , respectively. These regions could be responsible for the formation of hydrogen bonds at the active site of the corresponding receptor. The reactive sites of the title molecule were located with the help of the Multifunctional Wavefunction Analyzer (Lu & Chen, 2012). High positive potentials indicate regions with low electron density and a high probability of being attacked by a nucleophile. The positive regions in this molecule are around atoms H4A and H4B of the amino group, with MEP values of 34.833 and 33.040 kcal mol $^{-1}$ , respectively (Fig. 4). These electrostatic potential values can be used as predictors of chemical reactivity. The pyrimidine group, containing both proton-donating and proton-accepting sites, enables dimerization by formation of hydrogen bonds in the solid state, achieving N—H...N hydrogen-bond distances that are in the typical range of hydrogen bonds between aminopyrimidines. The values of the resulting electrostatic potentials in this molecular system make it possible to predict the formation of additional hydrogen bonds or the possible formation of covalent bonds in a synthesis process (Sarcher *et al.*, 2014).

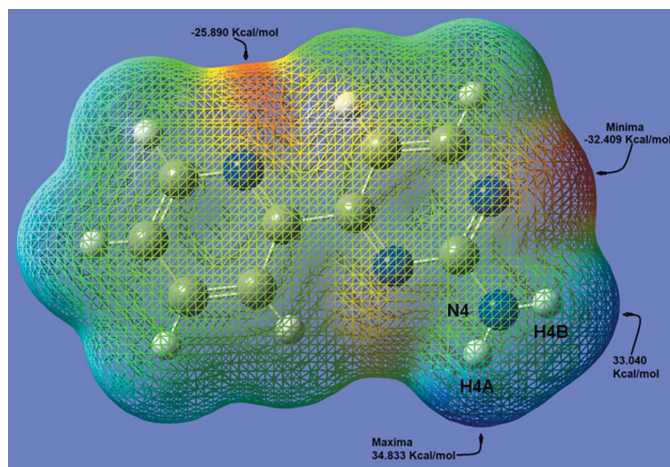


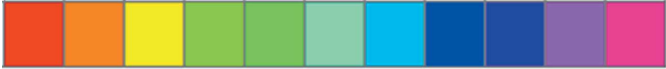
Figure 4

3D representation of the electrostatic potential around the molecule.



Table 3

Molecular pairs and interaction energies (kJ mol<sup>-1</sup>) obtained from the energy framework calculation for **PPA**.

										
Colour	N	Symmetry code	<i>R</i>	Electron density	<i>E</i> <sub>ele</sub>	<i>E</i> <sub>pol</sub>	<i>E</i> <sub>dis</sub>	<i>E</i> <sub>rep</sub>	<i>E</i> <sub>tot</sub>	
i	2	<i>x</i> , <i>y</i> , <i>z</i>	5.36	HF/3-21G	-3.2	-1.8	-35.3	17.8	-21.8	
ii	2	$-x + \frac{1}{2}, y + \frac{1}{2}, -z + \frac{1}{2}$	7.54	HF/3-21G	-3.4	-1.4	-16.2	12.6	-8.7	
iii	2	<i>x</i> , $-y, z + \frac{1}{2}$	6.88	HF/3-21G	-7.4	-1.5	-12.1	5.8	-14.7	
iv	1	$-x + \frac{1}{2}, -y + \frac{1}{2}, -z$	8.07	HF/3-21G	-7.5	-1.6	-10.5	4.8	-14.3	
v	1	$-x + \frac{1}{2}, -y + \frac{1}{2}, -z$	10.36	HF/3-21G	-0.5	-0.8	-8.9	5.0	-5.0	
vi	1	$-x, -y, -z$	6.66	HF/3-21G	-2.8	-1.2	-24.6	8.7	-18.8	
vii	1	$-x, y, -z + \frac{1}{2}$	7.56	HF/3-21G	-4.3	-1.1	-7.9	2.4	-10.3	
viii	2	<i>x</i> , $-y, z + \frac{1}{2}$	5.82	HF/3-21G	-10.7	-2.4	-22.5	17.3	-18.7	
ix	1	$-x, y, -z + \frac{1}{2}$	9.55	HF/3-21G	2.7	-0.8	-4.5	1.0	-1.0	
x	1	$-x, -y, -z$	9.39	HF/3-21G	-73.5	-22.4	-15.6	62.1	-53.2	
xi	2	<i>x</i> , $-y, z + \frac{1}{2}$	8.82	HF/3-21G	-4.0	-0.5	-5.5	2.5	-7.3	

Notes: scale factors used to determine *E*<sub>tot</sub>: *E*<sub>ele</sub> = 1.019, *E*<sub>pol</sub> = 0.651, *E*<sub>dis</sub> = 0.901 and *E*<sub>rep</sub> = 0.811. *R* is the distance between molecular centroids (Å). The colour bar indicates the colour-code interactive map for the first sphere of coordination around **PPA**.

Nucleophilic substitution reactions performed in our research group followed an effective path involving the amino functional group and resulted in the formation of new covalent bonds by integrating different heterocyclic rings into the reaction products. These compounds also show a trend in the crystalline state towards the generation of dimers, showing the formation of *R*<sub>2</sub><sup>2</sup>(8) synthons. A second polymorphic compound of **PPA**, which crystallizes in the monoclinic space group *P*2<sub>1</sub>/*c* with eight molecules in the unit cell, is reported in the literature (Bejan *et al.*, 1996). In the asymmetric unit, a dimerization by the formation of N—H...N hydrogen bonds, is observed. A study of the molecular electrostatic potential of the second polymorph showed equivalent values in regions of maximum and minimum potential that evidence the formation of new N—H...N interactions enhancing the formation of trimers or tetramers with *R*<sub>2</sub><sup>2</sup>(8) rings along [100]. The induc-

tion of these new N—H...N hydrogen bonds in a certain way inhibits, in the polymorph molecules, under solvent-free conditions, the creation of new relatively strong interactions, thereby reducing their reactivity with respect to the title **PPA** compound. In this way, the responsibility for suffering nucleophilic attacks, under the conditions that were previously established, must be focused on regions close to the pyridine N atoms.

### 3.5. 3D energy framework analysis

A more realistic interpretation of the molecular interactions in a crystalline compound can be achieved using the *Crystal-Explorer* program, which was inspired by the 'PIXEL' model of molecular interactions (Gavezzotti, 2005). Precise calculations, in which molecules are analyzed as a whole and not by

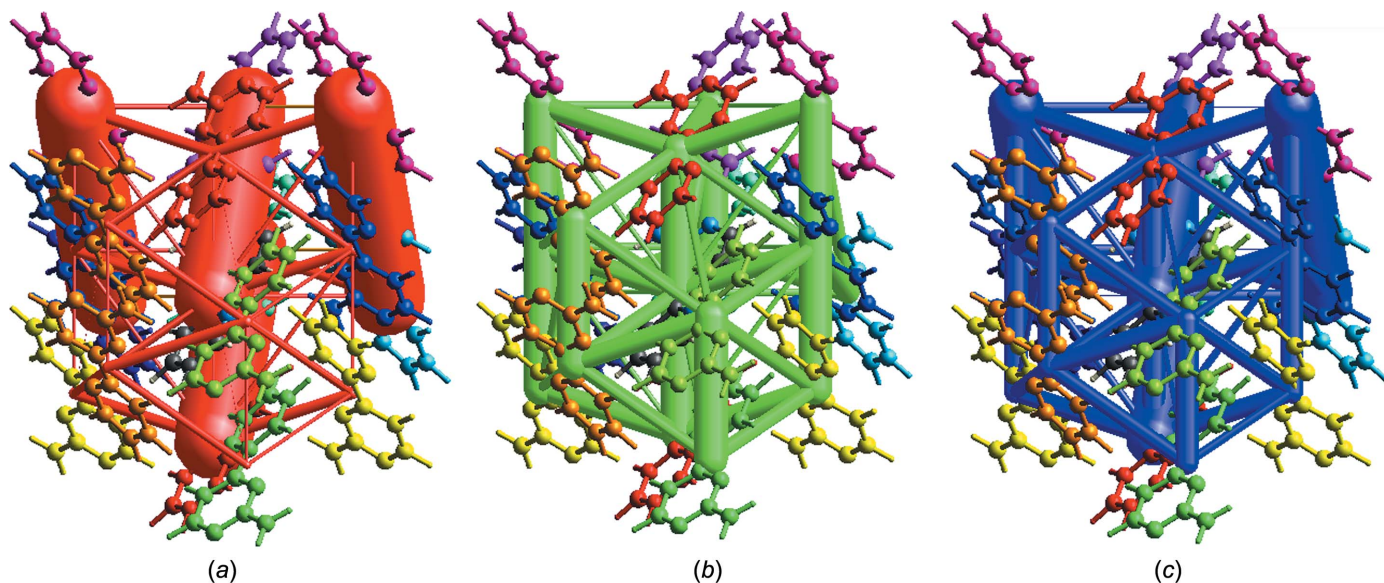


Figure 5

Energy frameworks corresponding to the different energy components, *i.e.* (a) electrostatic, (b) dispersion and (c) total energy framework, along the *b* axis. The tube size (scale factor) used in all the energy frameworks was 200.

calculations based on atom–atom contacts, were used, and these calculations considered interactions between pairs of molecules, and the energy values can be described according to Mackenzie *et al.* (2017) as the sum of the electrostatic ( $E_{\text{es}}$ ), polarization ( $E_{\text{pol}}$ ), dispersion ( $E_{\text{dis}}$ ) and exchange–repulsion ( $E_{\text{rep}}$ ) terms.

$$E_{\text{tot}} = E_{\text{es}} + E_{\text{pol}} + E_{\text{dis}} + E_{\text{rep}}$$

The interaction energies for the selected molecular pairs in the first sphere of coordination (radius 3.8 Å) around **PPA** are presented in Table 3.

The values of the interaction energies calculated between the pairs of molecules that appear in Table 4 and that are visualized in Fig. 5 show that one of the interactions with  $E_{\text{tot}} = -53.2 \text{ kJ mol}^{-1}$  contributes 31% of the total energy value and is related to pairs of molecules that are connected by N—H...N hydrogen bonds, and the distance  $R$  between their centroids is 9.39 Å. These interactions are represented predominantly by the term  $E_{\text{es}}$ , which is shown as the maximum term of this characteristic among all the interactions present. A second important contribution to the total energy is for pairs of related molecules with  $R = 5.36 \text{ Å}$  and  $E_{\text{tot}} = -21.8 \text{ kJ mol}^{-1}$ , and this interaction is mainly represented by the dispersion term ( $-35.3 \text{ kJ mol}^{-1}$ ) and involves mainly  $\pi$ – $\pi$  interactions.

Energy framework diagrams help clarify the crystal packing by combining efficient interactions with novel graphical representations, facilitating the visualization of the supra-molecular architecture of molecular structures. The global process of energetic interactions among pairs of **PPA** molecules is shown in Fig. 5, and the important contributions of the electrostatic term and the minor contribution of the dispersion term to the  $E_{\text{tot}}$  energy is shown. The results of the energy framework diagrams, indicated by the cylinders, reveal the directions of the interactions among the centroids of the molecules and their relative strengths in the molecular packing in different directions.

### 3.6. Vibrational analysis

To determine the spectroscopic behaviour of **PPA**, vibrational frequencies were calculated using the DFT/6-311G++(d,p) basis set. The theoretical and experimental Fourier transform IR (FT–IR) vibrational peaks are listed in Table 4. The differences between the calculated and experimental values are primarily due to the presence of inter-molecular interactions, including the formation of hydrogen bonds in the crystalline phase, and these interactions are not observed in the gas phase.

**3.6.1. N—H vibrations.** The N—H stretching vibration appears in the region  $3375 \pm 125 \text{ cm}^{-1}$  and the N—H deformation vibrations are in the regions 1510–1500, 1400–1300 and 740–730  $\text{cm}^{-1}$  (Socrates, 1981; Roeges, 1994). For the title molecule, potential energy distribution (PED) analysis gives the N—H symmetric stretching at  $3608 \text{ cm}^{-1}$ , and the N—H asymmetric stretch is observed at  $3736 \text{ cm}^{-1}$ . The experimental value for the symmetric stretching band is  $3296 \text{ cm}^{-1}$ ,

**Table 4**  
Vibrational assignments of **PPA**.

Assignations (PED %)	6311G++(d,p) ( $\text{cm}^{-1}$ ) Calculated	Exp FT–IR ( $\text{cm}^{-1}$ )
$\tau$ NCCC (88)	46	–
$\tau$ CNCN (74)	91	–
$\beta$ CCN (70)	142	–
$\tau$ CNCN (84)	190	–
$\tau$ CNCN (78)	232	–
$\nu$ CC (36) + $\beta$ CCN (26)	317	–
$\tau$ HNCN (90)	334	–
$\beta$ NCN (63)	360	–
$\tau$ CCCC (70)	415	–
$\tau$ CNCN (56)	444	–
$\beta$ CCN (42) + $\tau$ HNCN (37)	485	–
$\tau$ CCNC (63)	504	–
$\tau$ HNCN (58) + $\beta$ CCN (30)	524	–
$\beta$ CNC (66)	603	–
$\beta$ CCC (74)	639	650
$\beta$ CNC (72)	665	–
$\tau$ CCNC (62)	694	–
$\tau$ HCCC (53) + $\beta$ CNC (46) $\tau$ CNCC (25) + $\beta$ CCN (18)	764	783
$\tau$ HCCC (53) + $\beta$ CNC (46) + $\tau$ CNCC (25) + $\beta$ CCN (18)	764	–
$\tau$ CNCN (52) + $\tau$ CNCC (16) + $\tau$ HCCC (15)	811	804
$\tau$ HCCN (43) + $\tau$ CNCN (27) + $\tau$ HCCC (10)	825	–
$\tau$ HCCN (38) + $\tau$ CCNC (12) + $\tau$ HCNC (11) + $\tau$ CNCN (11)	877	847
$\tau$ HCCC (79)	929	–
$\nu$ NC (67)	945	926
$\tau$ HCCC (70) + $\tau$ CCCC (10)	989	–
$\beta$ CCN (18) + $\beta$ HCNC (41)	1008	–
$\beta$ CCN (13) + $\beta$ HCNC (29)	1008	995
$\beta$ CCC (55) + $\nu$ CC (21)	1014	–
$\tau$ HCCC (79) + $\tau$ CNCC (11)	1023	–
$\beta$ HNC (34) + $\beta$ CNC (13)	1043	–
$\nu$ CC (34) + $\beta$ CCC (19) + $\beta$ HCC (12)	1068	1094
$\nu$ NC (24) + $\beta$ HCN (17) + $\beta$ HCC (13)	1112	1103
$\beta$ CNC (22) + $\beta$ HCC (22) + $\nu$ CC (10)	1122	–
$\beta$ HCC (31) + $\beta$ HNC (21) + $\beta$ CNC (16)	1155	–
$\nu$ CC (15) + $\beta$ HCC (57)	1172	–
$\nu$ NC (70)	1257	1211
$\nu$ NC (49) + $\nu$ NC (10)	1288	1242
$\beta$ HCN (44) + $\nu$ NC (17)	1319	1302
$\beta$ HCN (20) + $\nu$ CC (15) + $\beta$ CCN (11)	1325	–
$\beta$ HCN (33) + $\nu$ CC (12)	1369	1342
$\beta$ HCC (42)	1461	1431
$\nu$ CC (21) + $\beta$ HCC (15)	1469	–
$\nu$ CN (26) + $\beta$ HCN (18) + $\delta$ HNH (13) + $\beta$ CCN (13)	1482	1464
$\beta$ HCC (43) + $\nu$ CC (16)	1508	–
$\nu$ CC (37)	1591	1545
$\nu$ CC (53)	1612	1566
$\nu$ CC (44) + $\delta$ HNH (11)	1621	–
$\nu$ CC (36) + $\delta$ HNH (13)	1629	1614
$\delta$ HNH (34) + $\nu$ NC (16)	1643	1651
$\nu$ CH (95)	3145	–
$\nu$ CH (91)	3146	3057
$\nu_{\text{as}}$ CH (79) + $\nu_{\text{s}}$ CH (18)	3173	3079
$\nu_{\text{s}}$ CH (78) + $\nu_{\text{as}}$ CH (17)	3193	3137
$\nu$ CH (99)	3220	–
$\nu$ CH (95)	3239	–
$\nu_{\text{s}}$ NH (100)	3608	3296
$\nu_{\text{as}}$ NH (100)	3736	3470

Notes:  $\nu$  = stretching,  $\beta$  = in-plane bending,  $\delta$  = scissoring,  $\gamma$  = out-of-plane bending,  $\tau$  = torsion vibration, s = symmetric and as = asymmetric.

and the asymmetric N—H stretch is at  $3470 \text{ cm}^{-1}$  (Fig. 3S in the supporting information). Pyridin-2-amine shows an experimental  $\nu_{\text{as}}$  N—H band at  $3445 \text{ cm}^{-1}$  (Büyükmurat *et al.*,

Table 5

Theoretical spectrum of the electronic absorption of **PPA** in the gas phase using TD-SCF B3LYP/6-311G++(d,p).

Transition	$\lambda_{\text{calc}}$ (nm)	$\lambda_{\text{exp}}$ (nm)	Oscillator strength	$E_{\text{HOMO}}$ (a.u.)	$E_{\text{LUMO}}$ (a.u.)	$E_{\text{HOMO-LUMO}}$ gap (a.u.)	Energy gap (eV)
I	316	323	0.0964	-0.22922	-0.06586	0.16336	4.4452
II	250	242	0.3648	-0.26322*	-0.06586	0.19736	5.3704
III	232	207	0.0295	-0.26322*	-0.0344**	0.22881	6.2262

Notes: (\*) HOMO-2; (\*\*) LUMO-1.

1999; Mary *et al.*, 2010). When comparing this value with the calculated value of the studied molecule, a red shift is observed (Athokpam *et al.*, 2017), perhaps caused by the formation of dimers involving N—H...N hydrogen bonds (Fig. 2). The existence of Nsp<sup>2</sup>—H...N hydrogen bonds in the **PPA** crystal was confirmed spectroscopically by its IR peaks due to the N—H stretching vibration shifting to lower wavenumbers in the solid state relative to those in the gas phase.

**3.6.2. C=C vibrations.** The ring C=C stretching vibrations were in the region 1400–1600 cm<sup>-1</sup>. In aromatic compounds such as pyridines, the strongest band is usually at approximately 1500 cm<sup>-1</sup> and the pyridin-2-amine C=C stretching band is present at approximately 1428–1584 cm<sup>-1</sup> (Büyükmurat *et al.*, 1999). Density functional theory (DFT) calculations showed aromatic C=C stretching modes in the 1469–1629 cm<sup>-1</sup> region.

**3.6.3. C—N vibrations.** The experimental C—N stretching band is at 1464 cm<sup>-1</sup>. The PED analysis shows a stretching band at 1482 cm<sup>-1</sup>. In pyridin-2-amine (Mary *et al.*, 2010), the C—NH<sub>2</sub> stretch occurs at 1325 cm<sup>-1</sup>. The theoretical scissoring vibrations occur at 1621, 1629 and 1643 cm<sup>-1</sup>, while the experimental IR spectrum shows the scissoring vibrations at 1614 and 1651 cm<sup>-1</sup>. The experimental values for pyridin-2-amine indicates that the IR scissoring mode occurs at 1627 cm<sup>-1</sup>. In turn, the C—N stretching vibrations are

observed at 1211, 1242 and 1302 cm<sup>-1</sup>. The DFT calculations give the C—N stretching bands at 1257, 1288 and 1319 cm<sup>-1</sup>.

**3.6.4. C—H vibrations.** The existence of one or more aromatic rings was confirmed by the C—H ring-related vibrations. The C—H stretching occurs above 3000 cm<sup>-1</sup> and appear as weak-to-moderate bands relative to the aliphatic bands. The experimental C—H stretching vibrations are at 3057, 3079 and 3137 cm<sup>-1</sup>, while the calculated values for the title molecule are at 3146, 3173 and 3193 cm<sup>-1</sup>. The calculated and experimental vibrational frequencies are generally in good agreement. No scaling factor for frequencies was used.

### 3.7. UV–Vis analysis

UV–Vis spectrophotometry, one of the most commonly used techniques in pharmaceutical chemistry, is used to determine the amount of UV or visible radiation absorbed by a substance in solution or in the solid state. Analysis of the frontier orbitals in a molecule may indicate how the molecule interacts with other species. A molecule with a small HOMO–LUMO energy gap (HOMO is the highest occupied molecular orbital and LUMO is the lowest unoccupied molecular orbital) is more polarizable and is generally more chemically reactive or less kinetically stable (Fleming, 1976). The electronic transition energies were determined using time-

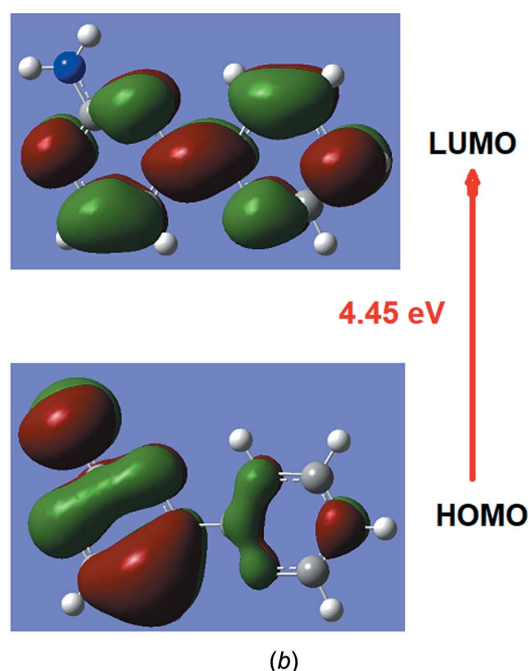
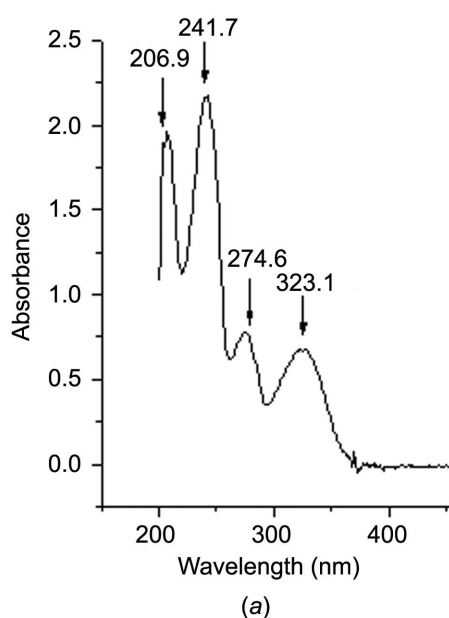


Figure 6

(a) UV–Vis absorption spectrum of **PPA**. (b) The frontier orbitals obtained with TD-DFT/6-311++G(d,p) (isovalue = 0.05).

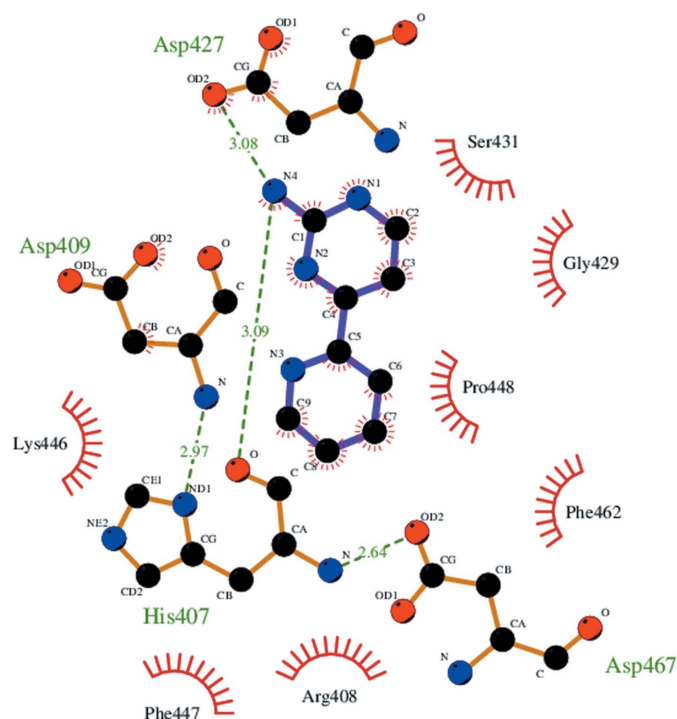


Figure 7

3D diagram of the interactions of compound **PPA** in the active site of tyrosine kinase (TK) showing two hydrogen bonds with Asp427 and His407. The atoms are coloured by atom type (carbon is black, nitrogen is blue and oxygen is red) and hydrogen bonds are represented by green dotted lines.

dependent density functional theory (TD-DFT) (Casida *et al.*, 1998) with the 6-311G++(d,p) basis set-optimized structure to evaluate the energetic capacity of the molecule. The probable excited states, theoretical electronic excitation energies, oscillator strengths and absorption wavelengths were evaluated. Table 5 shows the oscillator strength, the energy values of the HOMO and LUMO, as well as the HOMO–LUMO energy gap. The measured values of the absorption wavelengths ( $\lambda_{\text{max}}$ ) of **PPA** are shown in Fig. 6(a), and these values can be assigned to the  $\pi$ – $\pi^*$  transition (Gökce *et al.*, 2016).

From Fig. 6(b), it can be seen that the HOMO is uniformly distributed on the pyrimidine ring and the amino group, and that this orbital is partially distributed on the pyridine ring, whereas the LUMO is uniformly distributed on the pyrimidine and pyridine rings without any density on the amino group. This behaviour is consistent with a donor–acceptor unit, where the amino group acts as a donor and the pyridine and pyrimidine rings act as acceptors. The absorption of specific wavelengths in the UV–Vis region affects the appearance of the low electron-density zones in the molecule, which in this case correspond to the region close to the amino group.

Using the HOMO and LUMO orbital energies, the ionization energy and electron affinity can be expressed as  $I = -E_{\text{HOMO}}$  and  $A = -E_{\text{LUMO}}$ . The hardness,  $\eta$ , and chemical potential,  $\mu$ , can be found from the following relationships  $\eta = (I - A)/2$  and  $\mu = -(I + A)/2$ , where  $I$  and  $A$  are the first ionization potential and electron affinity of the chemical species, respectively (Parr & Pearson, 1983). Thus, for the

molecule under study,  $E_{\text{HOMO}} = -6.24$  eV,  $E_{\text{LUMO}} = -1.79$  eV, energy gap = 4.45 eV,  $I = 6.24$  eV,  $A = 1.79$  eV, global hardness  $\eta = 2.27$  eV,  $\mu = -4.02$  eV and global electrophilicity =  $\mu^2/2\eta = 3.56$  eV. The comparison of the results obtained in the analysis of the frontier orbitals with the results of the molecular electrostatic potentials (MEP) contributes to revealing possible properties of the molecule under study.

### 3.8. Molecular docking study

Since derivatives of the pyrimidine–pyridine fragment and structurally related compounds are well known as Bcr-Abl tyrosine kinase oncoprotein inhibitors, we decided to undertake a molecular docking study of one of the precursors in this series of inhibitors, **PPA**, into the binding site of the Bcr-Abl oncogene. PDB ID 3gvu was retrieved from the PDB (<http://www.rcsb.org/pdb>) for the docking studies; 3gvu has a good resolution of 2.05 Å. The enzyme has an attached cocrystallized inhibitor and therefore has a well-defined binding site. A molecular docking study was performed using *Auto Dock Vina* software (Trott & Olson, 2010). The protein–ligand interactions revealed a binding free energy  $\Delta G = -7.4$  kcal mol $^{-1}$ , showing a lower value than those of protein–pyrimidine derivatives, which have additional heterocycles and several functional groups in their structures. The docking results showed that the amino group of the pyrimidine moiety was simultaneously anchored by hydrogen-bonding interactions with Asp427 and His407 (Fig. 7).

A parallel molecular simulation work was also performed, where the **PPA** ligand interacted with the protein 2hyy, a protein that had originally been used in molecular simulation calculations with the compound imatinib, showing results similar to those found with the protein 3gvu.

## 4. Conclusions

The existence of dimers in the crystal is evidenced by the formation of  $R_2^2(8)$  N–H...N hydrogen-bonded rings, as well as by the shift of the N–H stretching vibration to lower wavenumbers in the solid state relative to those in the gas phase.

The calculation of the interaction energies between pairs of molecules visualized the electrostatic terms as the dominant factor against the dispersion factor in the crystal-growth process.

The molecule analyzed in this work is structurally distinct with respect to the position of the N atom in the pyridine ring compared with the structure of imatinib, an excellent inhibitor of Bcr-Abl tyrosine kinase. The interaction energies of this relatively small ligand in the active pocket of the protein indicate its potential and have inspired us to undertake a synthetic study to identify better pharmacophores against chronic myelogenous leukemia.

## Acknowledgements

RMF is grateful to Universidad del Valle for the support received for the realization of the CI 71073 project. The



authors also express their gratitude to Professor C. W. Lehmann of the Max-Planck-Institut für Kohlenforschung, Germany, for collection of the diffraction data.

### Funding information

Funding for this research was provided by: Universidad del Valle (grant No. 71073).

### References

- Agarwal, N., Raghuwanshi, S. K., Upadhyay, D. N., Shukla, P. K. & Ram, V. J. (2000). *Bioorg. Med. Chem. Lett.* **10**, 703–706.
- Amir, M., Javed, S. A. & Kumar, H. (2007). *Indian J. Pharm. Sci.* **69**, 337–343.
- Athokpam, B., Ramesh, S. & McKenzie, R. (2017). *Chem. Phys.* **488–489**, 43–54.
- Bailey, S. W. & Ayling, J. E. (2009). *Proc. Natl Acad. Sci.* **106**, 15424–15429.
- Becke, A. D. (1993). *J. Chem. Phys.* **98**, 1372–1377.
- Bejan, E., Haddou, H. A., Daran, J.-C. & Balavoine, G. G. A. (1996). *Synthesis*, **1996**, 1012–1018.
- Bettendorff, L., Mastrogiamco, F., Kish, S. J. & Grisar, T. (1996). *J. Neurochem.* **66**, 250–258.
- Bettendorff, L., Wirtzfeld, B., Makarchikov, A. F., Mazzucchelli, G., Frédrich, M., Gigliobianco, T., Gangolf, M., De Pauw, E., Angenot, L. & Wins, P. (2007). *Nat. Chem. Biol.* **3**, 211–212.
- Brown, D. J. (2009). In *The Chemistry of Heterocyclic Compounds, The Pyrimidines*. New York: John Wiley and Sons.
- Bruker (2006). *DATCOL*. Bruker AXS Inc., Madison, Wisconsin, USA.
- Bruker (2012). *SADABS*. Bruker AXS Inc., Madison, Wisconsin, USA.
- Büyükmurat, Y., Akalin, E., Özel, A. & Akyüz, S. (1999). *J. Mol. Struct.* **482–483**, 579–584.
- Casida, M. E., Jamorski, C., Casida, K. C. & Salahub, D. R. (1998). *J. Chem. Phys.* **108**, 4439–4449.
- Chahwan, R., Wontakal, S. N. & Roa, S. (2010). *Trends Genet.* **26**, 443–448.
- Duisenberg, A. J. M., Kroon-Batenburg, L. M. J. & Schreurs, A. M. M. (2003). *J. Appl. Cryst.* **36**, 220–229.
- Farrugia, L. J. (2012). *J. Appl. Cryst.* **45**, 849–854.
- Fleming, I. (1976). In *Frontier Orbitals and Organic Chemical Reactions*. New York: John Wiley and Sons.
- Gavezzotti, A. (2005). *Z. Kristallogr.* **220**, 499–510.
- Gökce, H., Öztürk, N., Ceylan, Ü., Alpaslan, Y. B. & Alpaslan, G. (2016). *Spectrochim. Acta A Mol. Biomol. Spectrosc.* **163**, 170–180.
- Jamróz, M. H. (2013). *Spectrochim. Acta A Mol. Biomol. Spectrosc.* **114**, 220–230.
- Joule, J. A. & Mills, K. (2010). Editors. *Heterocyclic Chemistry*, 5th ed. Oxford: Wiley.
- Lee, C., Yang, W. & Parr, R. G. (1988). *Phys. Rev. B*, **37**, 785–789.
- Lu, T. & Chen, F. (2012). *J. Comput. Chem.* **33**, 580–592.
- Mackenzie, C. F., Spackman, P. R., Jayatilaka, D. & Spackman, M. A. (2017). *IUCrJ*, **4**, 575–587.
- Macrae, C. F., Bruno, I. J., Chisholm, J. A., Edgington, P. R., McCabe, P., Pidcock, E., Rodriguez-Monge, L., Taylor, R., van de Streek, J. & Wood, P. A. (2008). *J. Appl. Cryst.* **41**, 466–470.
- Mary, Y. S., Panicker, C. Y. & Varghese, H. T. (2010). *Int. J. Chem. Sci.* **8**, 1071–1076.
- McKinnon, J. J., Spackman, M. A. & Mitchell, A. S. (2004). *Acta Cryst.* **B60**, 627–668.
- Nakamura, N., Okawa, H., Inazu, T. & Kida, S. (1982). *Bull. Chem. Soc. Jpn.* **55**, 2400–2403.
- Nielsen, A. B. & Holder, A. J. (2009). *GaussView 5.0*. Gaussian Inc., Pittsburgh, USA. <https://gaussian.com/gaussview6/>.
- Padwa, A., Woolhouse, A. D., Katritzky, A. R. & Rees, C. W. (1984). In *Comprehensive Heterocyclic Chemistry*. Oxford University Press.
- Parr, R. G. & Pearson, R. G. (1983). *J. Am. Chem. Soc.* **105**, 7512–7516.
- Porter, A. E. A. (1979). In *Diazines and Benzodiazines*, Vol. 14, Oxford: Pergamon Press; Amsterdam: Elsevier Science BV.
- Rana, K., Kaur, B. & Kumar, B. (2004). *Indian J. Chem. Sect. B*, **43**, 1553–1557.
- Roeges, N. P. G. (1994). In *A Guide to Complete Interpretation of Infrared Spectra of Organic Structures*. New York: Wiley.
- Sakaki, S., Kato, K., Miyazaki, T., Musashi, Y., Ohkubo, K., Ihara, H. & Hirayama, C. (1993). *J. Chem. Soc. Faraday Trans.* **89**, 659–664.
- Sarcher, C., Farsadpour, S., Taghizadeh Ghoochany, L., Sun, Y., Thiel, W. R. & Roesky, P. W. (2014). *Dalton Trans.* **43**, 2397–2405.
- Sharma, P., Rane, N. & Gurram, V. K. (2004). *Bioorg. Med. Chem. Lett.* **14**, 4185–4190.
- Sheldrick, G. M. (2015a). *Acta Cryst.* **A71**, 3–8.
- Sheldrick, G. M. (2015b). *Acta Cryst.* **C71**, 3–8.
- Socrates, G. (1981). In *Infrared Characteristic Group Frequencies*. New York: John Wiley and Sons.
- Sondhi, S. M., Jain, S., Dwivedi, A. D., Shukla, R. & Raghubir, R. (2008). *Indian J. Chem. Sect. B*, **47**, 136–143.
- Spackman, M. A. & Jayatilaka, D. (2009). *CrystEngComm*, **11**, 19–32.
- Trott, O. & Olson, A. J. (2010). *J. Comput. Chem.* **31**, 455–461.
- Turro, N. J. (2005). *PNAS*, **102**, 10766–10770.
- Xie, F., Zhao, H., Zhao, L., Lou, L. & Hu, Y. (2009). *Bioorg. Med. Chem. Lett.* **19**, 275–278.
- Zajac, M. A., Zakrzewski, A. G., Kowal, M. G. & Narayan, S. (2003). *Synth. Commun.* **33**, 3291–3297.
- Zempleni, J., Galloway, J. R. & McCormick, D. B. (1996). *Am. J. Clin. Nutr.* **63**, 54–66.

## supporting information

*Acta Cryst.* (2019). C75, 1681-1689 [https://doi.org/10.1107/S2053229619015523]

## Synthesis, spectroscopic (FT–IR and UV–Vis), crystallographic and theoretical studies, and a molecular docking simulation of an imatinib-like template

**Rodolfo Moreno-Fuquen, Kevin Arango-Daraviña, Esteban Garcia, Juan-C. Tenorio and Javier Ellena**

### Computing details

Data collection: *DATCOL* (Bruker, 2006); cell refinement: *EVALCCD* (Duisenberg *et al.*, 2003); data reduction: *EVALCCD* (Duisenberg *et al.*, 2003); program(s) used to solve structure: *SHELXT* (Sheldrick, 2015a); program(s) used to refine structure: *SHELXL2014* (Sheldrick, 2015b); molecular graphics: *ORTEP-3* (Farrugia, 2012), *Mercury* (Macrae *et al.*, 2008) and *CrystalExplorer* (McKinnon *et al.*, 2004); software used to prepare material for publication: *SHELXL2014* (Sheldrick, 2015b).

### 4-(Pyridin-2-yl)pyrimidin-2-amine

#### Crystal data

$C_9H_8N_4$	$D_x = 1.388 \text{ Mg m}^{-3}$
$M_r = 172.19$	Melting point: 413 K
Monoclinic, $I2/a$	Mo $K\alpha$ radiation, $\lambda = 0.71073 \text{ \AA}$
$a = 11.4608 (15) \text{ \AA}$	Cell parameters from 4441 reflections
$b = 5.3791 (9) \text{ \AA}$	$\theta = 3.1\text{--}30.0^\circ$
$c = 26.740 (4) \text{ \AA}$	$\mu = 0.09 \text{ mm}^{-1}$
$\beta = 91.457 (12)^\circ$	$T = 293 \text{ K}$
$V = 1647.9 (4) \text{ \AA}^3$	Block, colourless
$Z = 8$	$0.40 \times 0.23 \times 0.20 \text{ mm}$
$F(000) = 720$	

#### Data collection

Bruker Enraf–Nonius KappaCCD diffractometer	4441 measured reflections
Radiation source: $0.2 \times 2 \text{ mm}^2$ focus rotating anode	2379 independent reflections
Detector resolution: $18.02 \text{ pixels mm}^{-1}$	1688 reflections with $I > 2\sigma(I)$
CCD $\varphi$ - and $\omega$ -scans	$R_{\text{int}} = 0.020$
Absorption correction: gaussian (SADABS; Bruker, 2012)	$\theta_{\text{max}} = 30.0^\circ$ , $\theta_{\text{min}} = 3.1^\circ$
$T_{\text{min}} = 0.624$ , $T_{\text{max}} = 0.995$	$h = -16 \rightarrow 11$
	$k = -7 \rightarrow 7$
	$l = -31 \rightarrow 37$

#### Refinement

Refinement on $F^2$	2379 reflections
Least-squares matrix: full	126 parameters
$R[F^2 > 2\sigma(F^2)] = 0.046$	0 restraints
$wR(F^2) = 0.134$	Hydrogen site location: mixed
$S = 1.03$	

H atoms treated by a mixture of independent  
and constrained refinement  
 $w = 1/[\sigma^2(F_o^2) + (0.0583P)^2 + 0.5919P]$   
where  $P = (F_o^2 + 2F_c^2)/3$

$$(\Delta/\sigma)_{\max} < 0.001$$

$$\Delta\rho_{\max} = 0.22 \text{ e } \text{\AA}^{-3}$$

$$\Delta\rho_{\min} = -0.22 \text{ e } \text{\AA}^{-3}$$

#### Special details

**Geometry.** All esds (except the esd in the dihedral angle between two l.s. planes) are estimated using the full covariance matrix. The cell esds are taken into account individually in the estimation of esds in distances, angles and torsion angles; correlations between esds in cell parameters are only used when they are defined by crystal symmetry. An approximate (isotropic) treatment of cell esds is used for estimating esds involving l.s. planes.

**Refinement.** The crystal structure was solved with SHELXT (Sheldrick, 2014) and refined with SHELXL (Sheldrick, 2014). Anisotropic atomic displacement parameters were introduced for all non-hydrogen atoms.

Structure pictures were drawn with ORTEP (Farrugia, 2012), Mercury (Macrae *et al.*, 2008) and CrystalExplorer (McKinnon *et al.*, 2004).

#### Fractional atomic coordinates and isotropic or equivalent isotropic displacement parameters ( $\text{\AA}^2$ )

	x	y	z	$U_{\text{iso}}^*/U_{\text{eq}}$
N1	0.59793 (10)	0.8075 (2)	0.54174 (4)	0.0397 (3)
N2	0.49244 (9)	0.4940 (2)	0.58498 (4)	0.0334 (3)
N3	0.67213 (11)	0.1998 (3)	0.67891 (5)	0.0475 (3)
N4	0.40143 (12)	0.7523 (3)	0.52808 (5)	0.0458 (3)
C1	0.50044 (11)	0.6820 (3)	0.55227 (5)	0.0336 (3)
C2	0.69358 (12)	0.7359 (3)	0.56694 (5)	0.0444 (4)
H2	0.763316	0.816777	0.560470	0.053*
C3	0.69520 (12)	0.5499 (3)	0.60189 (5)	0.0411 (3)
H3	0.763313	0.505318	0.619289	0.049*
C4	0.58989 (11)	0.4316 (2)	0.60997 (5)	0.0320 (3)
C5	0.58070 (11)	0.2278 (2)	0.64725 (5)	0.0325 (3)
C6	0.48303 (12)	0.0784 (3)	0.64859 (5)	0.0369 (3)
H6	0.420375	0.105298	0.626471	0.044*
C7	0.47957 (13)	−0.1109 (3)	0.68304 (5)	0.0420 (3)
H7	0.415261	−0.215904	0.684306	0.050*
C8	0.57305 (14)	−0.1415 (3)	0.71553 (6)	0.0476 (4)
H8	0.573555	−0.268033	0.739234	0.057*
C9	0.66543 (14)	0.0180 (3)	0.71233 (6)	0.0540 (4)
H9	0.727581	−0.002133	0.735011	0.065*
H4A	0.3371 (19)	0.677 (4)	0.5350 (7)	0.066 (6)*
H4B	0.4016 (15)	0.880 (4)	0.5056 (7)	0.057 (5)*

#### Atomic displacement parameters ( $\text{\AA}^2$ )

	$U^{11}$	$U^{22}$	$U^{33}$	$U^{12}$	$U^{13}$	$U^{23}$
N1	0.0365 (6)	0.0410 (7)	0.0416 (6)	−0.0022 (5)	0.0005 (5)	0.0065 (5)
N2	0.0286 (5)	0.0365 (6)	0.0349 (5)	0.0018 (5)	−0.0007 (4)	0.0024 (4)
N3	0.0353 (6)	0.0509 (8)	0.0555 (7)	−0.0016 (6)	−0.0114 (5)	0.0148 (6)
N4	0.0347 (7)	0.0508 (8)	0.0516 (7)	0.0001 (6)	−0.0058 (5)	0.0169 (6)
C1	0.0319 (6)	0.0356 (7)	0.0332 (6)	0.0022 (5)	0.0003 (5)	−0.0010 (5)
C2	0.0322 (7)	0.0519 (9)	0.0492 (8)	−0.0066 (7)	0.0000 (6)	0.0087 (7)

C3	0.0281 (6)	0.0491 (9)	0.0457 (7)	−0.0006 (6)	−0.0036 (5)	0.0081 (6)
C4	0.0285 (6)	0.0347 (7)	0.0329 (6)	0.0025 (5)	0.0010 (4)	−0.0003 (5)
C5	0.0289 (6)	0.0344 (7)	0.0343 (6)	0.0035 (5)	−0.0004 (4)	0.0005 (5)
C6	0.0329 (6)	0.0405 (8)	0.0372 (6)	−0.0005 (6)	−0.0021 (5)	−0.0017 (6)
C7	0.0411 (7)	0.0396 (8)	0.0457 (7)	−0.0040 (6)	0.0058 (6)	0.0007 (6)
C8	0.0503 (9)	0.0425 (8)	0.0500 (8)	0.0030 (7)	0.0020 (6)	0.0132 (7)
C9	0.0449 (8)	0.0565 (10)	0.0599 (9)	0.0017 (8)	−0.0150 (7)	0.0196 (8)

*Geometric parameters (Å, °)*

N1—C2	1.3291 (17)	C3—C4	1.3862 (19)
N1—C1	1.3413 (18)	C3—H3	0.9300
N2—C4	1.3297 (16)	C4—C5	1.4875 (18)
N2—C1	1.3420 (17)	C5—C6	1.3792 (19)
N3—C9	1.3286 (19)	C6—C7	1.374 (2)
N3—C5	1.3386 (16)	C6—H6	0.9300
N4—C1	1.3459 (17)	C7—C8	1.372 (2)
N4—H4A	0.87 (2)	C7—H7	0.9300
N4—H4B	0.91 (2)	C8—C9	1.367 (2)
C2—C3	1.369 (2)	C8—H8	0.9300
C2—H2	0.9300	C9—H9	0.9300
C2—N1—C1	115.38 (12)	C3—C4—C5	121.30 (11)
C4—N2—C1	116.56 (11)	N3—C5—C6	122.74 (12)
C9—N3—C5	116.77 (13)	N3—C5—C4	116.04 (12)
C1—N4—H4A	118.6 (13)	C6—C5—C4	121.22 (11)
C1—N4—H4B	120.8 (11)	C7—C6—C5	119.10 (12)
H4A—N4—H4B	120.6 (18)	C7—C6—H6	120.4
N1—C1—N2	125.95 (12)	C5—C6—H6	120.4
N1—C1—N4	117.02 (13)	C8—C7—C6	118.56 (14)
N2—C1—N4	117.03 (12)	C8—C7—H7	120.7
N1—C2—C3	123.68 (13)	C6—C7—H7	120.7
N1—C2—H2	118.2	C9—C8—C7	118.59 (14)
C3—C2—H2	118.2	C9—C8—H8	120.7
C2—C3—C4	116.43 (12)	C7—C8—H8	120.7
C2—C3—H3	121.8	N3—C9—C8	124.21 (14)
C4—C3—H3	121.8	N3—C9—H9	117.9
N2—C4—C3	121.97 (12)	C8—C9—H9	117.9
N2—C4—C5	116.73 (11)		
C2—N1—C1—N2	−0.6 (2)	C9—N3—C5—C4	−179.77 (13)
C2—N1—C1—N4	178.87 (13)	N2—C4—C5—N3	−167.20 (12)
C4—N2—C1—N1	1.8 (2)	C3—C4—C5—N3	12.78 (19)
C4—N2—C1—N4	−177.71 (12)	N2—C4—C5—C6	12.77 (19)
C1—N1—C2—C3	−0.8 (2)	C3—C4—C5—C6	−167.24 (13)
N1—C2—C3—C4	0.9 (2)	N3—C5—C6—C7	−1.4 (2)
C1—N2—C4—C3	−1.58 (19)	C4—C5—C6—C7	178.66 (12)
C1—N2—C4—C5	178.40 (11)	C5—C6—C7—C8	1.1 (2)



C2—C3—C4—N2	0.4 (2)	C6—C7—C8—C9	0.2 (2)
C2—C3—C4—C5	−179.61 (13)	C5—N3—C9—C8	1.2 (3)
C9—N3—C5—C6	0.2 (2)	C7—C8—C9—N3	−1.4 (3)

*Hydrogen-bond geometry (Å, °)*

<i>D</i> —H $\cdots$ <i>A</i>	<i>D</i> —H	H $\cdots$ <i>A</i>	<i>D</i> $\cdots$ <i>A</i>	<i>D</i> —H $\cdots$ <i>A</i>
N4—H4B $\cdots$ N1 <sup>i</sup>	0.91 (2)	2.10 (2)	3.0154 (19)	175.8 (16)

Symmetry code: (i)  $-x+1, -y+2, -z+1$ .